This article has been accepted for publication in IEEE Transactions on Antennas and Propagation. This is the author's version which has not been fully edited and content may change prior to final publication. Citation information: DOI 10.1109/TAP.2025.3572609

Ray Paths and Frequency Dependence of Mismatched Luneburg Lenses

Vincent Kaschten, *Member, IEEE,* Dimitri Lederer, *Member, IEEE,* and Christophe Craeye, *Senior Member, IEEE*

***Abstract*—The recently introduced *Mismatched Luneburg Lenses* are studied with an in-depth analysis regarding their frequency dependence. This article proposes an analytical expression of the ray paths inside such lenses, which is then used to derive a radiation integral. The effect of the mismatch appears to be frequency-dependent, and an expression for the optimal homogeneous lens is given as a function of frequency. The previously proposed law linking the refractive index at the lens center and the lens edge is now modified into a generalized rule, taking into account that frequency dependence.**

***Index Terms*—gradient-index (GRIN) lenses, Luneburg lens, Gutman lens, homogeneous lens, ray path, collimation, physical optics, radiation integral, GRIN effect, interface effect.**

I. Introduction

In 1944, R. K. Luneburg [1] published an analytical solution for the refractive index distribution $n(r) = \sqrt{2-(r/R)^2}$ to be implemented along the radial coordinate r of a spherical lens, for the lens to feature a focus on its surface ($r = R$) and another one diametrically opposite, at infinity. This paved the way to numerous applications taking advantage of

- its angular selectivity, with applications such as direction-finding at Ka-band [2], direction cloaking [3] or low-cost beamformer at millimeter-wave bands [4];
- its very low scan losses, with applications such as multi-beam antenna at sub-THz frequencies [5] or even full-angle operation at C-band [6];
- its true time delay nature making it ultra-wideband, with applications such as antenna for high data rates at Ka-band [7] or covering the whole D-band [8].

In parallel to these practical implementations of Luneburg lenses, theoretical work has also been conducted to study the lens behaviour and its possible adaptations.

In 1954, A. S. Gutman [9] showed how to adapt the Luneburg lens in order to have the focus at radial position $f \leq R$ on the inside of the lens, while still using the full aperture. By means of Hamiltonian optics in Cartesian coordinates, he showed that the distributions should be adapted to $n(r) = \sqrt{1+(R/f)^2-(r/f)^2}$ and that the trajectories of the rays inside such a lens can be described by a family of ellipses passing through the focal point:

$$x(y) = y\ \frac{\cos\alpha}{\sin\alpha} \pm f\sqrt{1-\left(\frac{y}{R\ \sin\alpha}\right)^2} \tag{1}$$

where α is the initial angle of the ray trajectory with respect to the main axis.

In 2008, J. A. Lock [10] applied the conservation of the angular momentum to the classical Luneburg lens: the general equation of an ellipse was used to describe the path, the ellipse was then rotated with respect to the lens main axis, and its parameters were obtained by applying boundary conditions. The ray trajectory in polar coordinates is then given by

$$r(\theta) = \frac{R\ \sin\alpha}{\sqrt{1-\cos\alpha\ \cos(2\theta+\alpha)}} \tag{2}$$

In 2019, C. Babayigit et al. [3] derived the ray trajectory equation in Cartesian coordinates for the classical Luneburg lens with any initial position (x_0,y_0) and initial angle α. They used the optical path length of a ray and applied Fermat's principle and boundary conditions.

In 2021, J. Ruiz-García et al. [11] proposed a new type of lens called the *Reflecting Luneburg Lens*, and in particular a closed form formulation of the ray paths, obtained through first computing the turning point r_{min}, i.e. the point of the ray path closest to the center of the lens, and then using it to rewrite the ray path in an integral form.

In 2024, the authors of this paper [12] proposed to drop the constraint that the Luneburg lens be matched with its exterior medium and introduced the *Mismatched Luneburg Lenses* following a refractive index distribution

$$n^2(r) = \varepsilon_r(r) = \varepsilon_{center} - (\varepsilon_{center} - \varepsilon_{edge})\ \left(\frac{r}{R}\right)^2 \tag{3}$$

with the parameters $\varepsilon_{center}, \varepsilon_{edge} \geq 1$ representing the relative dielectric permittivity at the lens center and edge, respectively. A comprehensive analysis was carried out based on numerical methods, including methods relying on geometrical optics such as Abbe's refraction invariant (leading to the relation $\varepsilon_{center} = 2\sqrt{\varepsilon_{edge}}$) and ray tracing (leading to the relation $\varepsilon_{center} = 2+\sqrt{2}(\sqrt{\varepsilon_{edge}}-1)$, confirmed by 2D full-wave simulations), however without analytically obtaining the ray trajectories inside such lenses. Those lenses obtained through numerical optimizations of the generalized Luneburg problem consequently exhibit aberrations.

Manuscript received 10 July 2023; revised 5 February 2024; accepted 20 February 2024. Date of publication 19 March 2024; date of current version 7 May 2024. This work was supported by the Région Wallonne through the "Doctorat en entreprise" Framework of the Service Public de Wallonie (SPW) Economie, Emploi, Recherche. (*Corresponding author: Vincent Kaschten.*)

Vincent Kaschten is with the Institute of Information and Communication Technologies, Electronics and Applied Mathematics (ICTEAM), Universite catholique de Louvain, 1348 Louvain-la-Neuve, Belgium, and also with BEA Sensors, 4031 Liège, Belgium (e-mail: vincent.kaschten@uclouvain.be). Dimitri Lederer and Christophe Craeye are with the Institute of Information and Communication Technologies, Electronics and Applied Mathematics (ICTEAM), Universite catholique de Louvain, 1348 Louvain-la-Neuve, Belgium.

Color versions of ne or more figures in this article are available at https://doi.org/10.1109/TAP.2024.3376725.

Digital Object Identifier 10.1109/TAP.2024.3376725

Authorized licensed use limited to: Univ Catholique de Louvain/UCL. Downloaded on June 24,2025 at 12:01:17 UTC from IEEE Xplore. Restrictions apply.
© 2025 IEEE. All rights reserved, including rights for text and data mining and training of artificial intelligence and similar technologies. Personal use is permitted, but republication/redistribution requires IEEE permission. See https://www.ieee.org/publications/rights/index.html for more information.

This article has been accepted for publication in IEEE Transactions on Antennas and Propagation. This is the author's version which has not been fully edited and content may change prior to final publication. Citation information: DOI 10.1109/TAP.2025.3572609

That same year, and in a same attempt to facilitate the practical realization of Luneburg lenses and increase design flexibility, O. Zetterstrom et al. [13] proposed to combine the principles of a virtual image lens – introduced in 2021 by N. J. G. Fonseca et al. [14] – and an extended hemispherical lens, leading to the so-called *Collimating Truncated Virtual Image Lens*, resulting in a mismatched lens as well. Aberrations arise since the perfectly collimating elliptical edge is truncated into a spherical edge, although this approximation is rather accurate. In both cases [12][13], little has been said about the frequency dependence of such lenses. Phase aberrations have already been highlighted long time ago for homogeneous dielectric lenses [15].

The objective of this article is first to obtain an analytical expression for the ray paths inside a *Mismatched Luneburg Lens* fed on its perimeter. Note that the lenses considered in this work are cylindrical. Section II proposes a straightforward derivation method based on the conservation of the angular momentum, while Section III generalizes the developments of Gutman [9]. This article also aims at providing a quantitative analysis of the lenses under study. Section IV uses the obtained ray paths to derive a 2D radiation integral, based on physical optics, and it highlights the frequency dependence of *Mismatched Luneburg Lenses*. Section V compares the proposed lenses with those described in [13], at various frequencies through 3D full-wave simulations.

II. New Derivation of the Ray Path

In this paper we want to study distributions which result in a lens that is not necessarily matched [12] with the exterior medium. For the sake of simplification, let us rewrite (3) as

$$n^2(r) = a - br^2 \tag{4}$$

with $a = \varepsilon_{center}$ and $b = \varepsilon_{center} - \varepsilon_{edge}$ and assume a normalized lens radius $R = 1$. In polar coordinates (r, θ) a ray trajectory is characterized by an angular momentum L [11] such that

$$d\theta = \frac{\pm\, L dr}{r\sqrt{n^2(r)r^2 - L^2}} \tag{5}$$

with $L = r\ n(r)\ \sin\psi = \sqrt{a-b}\ \sin\alpha$ the quantity that is preserved throughout the whole ray path and ψ the angle between the ray local orientation (tangent $\vec{t}$ to the ray path) and the position vector $\vec{r}$, see Fig. 1 for the different notations. The sign in (5) depends on the angle ψ, with a $-$ sign when $\psi \leq \pi/2$ and a $+$ sign when $\psi \geq \pi/2$.

The differential equation (5) can be rewritten with the distributions (4) under study, and integrated side by side:

$$\int \frac{d\theta}{dr} dr = \int \frac{\pm\ L\ dr}{r\sqrt{(a-br^2)r^2 - L^2}} \tag{6}$$

The right-hand side has an analytical solution:

$$f(r) = \frac{1}{2}\tan^{-1}\left(\frac{ar^2 - 2L^2}{2L\sqrt{ar^2 - br^4 - L^2}}\right) \tag{7}$$

We thus know that everywhere, the ray path $\theta(r)$ will simply be given by $\theta(r) = \pm f(r) + C$ with a constant C to be determined based on the boundary conditions. As in [11], we use the point of the ray path $r = r_{min}$ closest to the center of the lens and where $\psi = \pi/2$. We can deduce its value by applying the conservation of the angular momentum:

$$L = r_{min}\ \sqrt{a - br_{min}^2} \Leftrightarrow r_{min} = \frac{a - \sqrt{a^2 - 4bL^2}}{2b} \tag{8}$$

With (8) inserted in (7) one observes that

$$f(r_{min}) = \frac{\pi}{4} \tag{9}$$

while the evaluation of $f(r)$ in $r = 1$ can be rewritten, using the angular momentum in the form $L = \sqrt{\varepsilon_{edge}}\sin\alpha$, as

$$f(r=1) = \frac{1}{2}\tan^{-1}\left(\frac{\varepsilon_{center} - 2\varepsilon_{edge}\sin^2\alpha}{2\varepsilon_{edge}\sin\alpha\cos\alpha}\right) \tag{10}$$

The first part of the ray path $\theta_1(r)$ goes from $(r = 1, \theta = 0)$ to $(r = r_{min}, \theta = \theta_{min})$ where $\psi \leq \pi/2$, while the second part of the ray path $\theta_2(r)$ goes from $(r = r_{min}, \theta = \theta_{min})$ to $(r = 1, \theta = \theta_{end})$ where $\psi \geq \pi/2$, such that

$$\boxed{\begin{cases} \theta_1(r) = -f(r) + f(r=1) \\ \theta_2(r) = +f(r) - f(r=r_{min}) + \theta_{min} \end{cases}} \tag{11}$$

With that expression it is possible to compute

$$\begin{cases} \theta_{min} = \theta_1(r_{min}) = -f(r=r_{min}) + f(r=1) \\ \theta_{end} = \theta_2(r=1) = 2\theta_{min} \end{cases} \tag{12}$$

and taking the tangent of both sides of (12), one gets

$$\tan\theta_{end} = \frac{-1}{\tan\left(2f(r=1)\right)} = \frac{-2\varepsilon_{edge}\sin\alpha\cos\alpha}{\varepsilon_{center} - 2\varepsilon_{edge}\sin^2\alpha} \tag{13}$$

Because the quantity L is conserved during the whole path, we know that $\sin\phi_{final,in} = \sin\alpha$ and the refraction law at the lens edge allows us to write

$$\phi_{final,out} = \sin^{-1}\left(\sqrt{\varepsilon_{edge}}\ \sin\alpha\right) \tag{14}$$

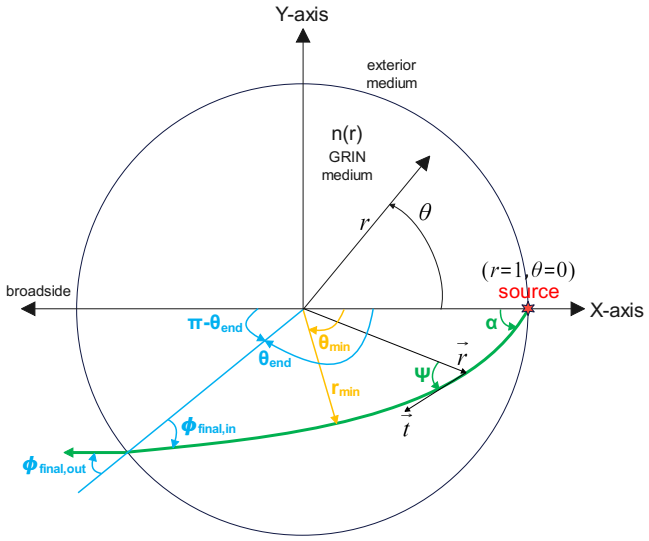

Fig. 1. Ray path geometry in a mismatched Luneburg lens. A ray path (green curve) starts with an initial angle α with respect to the main X-axis (broadside), reaches a position of minimum radius r_{min} at angular position θ_{min}, and eventually exits the lens at angular position θ_{end}. There, refraction takes place in case of mismatch, resulting in $\phi_{final,out} \neq \phi_{final,in}$.

Authorized licensed use limited to: Univ Catholique de Louvain/UCL. Downloaded on June 24,2025 at 12:01:17 UTC from IEEE Xplore. Restrictions apply.
© 2025 IEEE. All rights reserved, including rights for text and data mining and training of artificial intelligence and similar technologies. Personal use is permitted, but republication/redistribution requires IEEE permission. See https://www.ieee.org/publications/rights/index.html for more information.

This article has been accepted for publication in IEEE Transactions on Antennas and Propagation. This is the author's version which has not been fully edited and content may change prior to final publication. Citation information: DOI 10.1109/TAP.2025.3572609

The orientation with respect to broadside, i.e. once the ray has exited the lens and undergone the last refraction between the lens edge and the exterior medium, is given by the "orientation"

$$or = (\pi - \theta_{end}) - \phi_{final,out} \tag{15}$$

and only depends on the values $(\varepsilon_{center}, \varepsilon_{edge})$ and α through expressions (12) and (14). It is therefore very efficiently computed. Previously in [12], those ray trajectories were determined iteratively by use of ray tracing, by minimizing the standard deviation of the *or* under the same definition as (15). This led to an empirical rule

$$\varepsilon_{center} = 2 + \sqrt{2}\ (\sqrt{\varepsilon_{edge}} - 1) \tag{16}$$

providing optimal lens distributions with maximal gain at broadside, as confirmed by full-wave simulations at 60 GHz with a lens diameter $D = 30$ mm. The ray paths for the first and second parts (11) are represented as orange trajectories in Fig. 2 for various lenses obeying (16), while the green trajectories outside the lenses are obtained by computing the *or* (15). An analytically equivalent but geometrically more insightful expression of the ray paths will be derived in section III.

III. Truncated Gutman lenses

In this section, we apply Gutman's method [9] to obtain the ray paths inside a GRIN lens obeying (4) with $r^2 = x^2 + y^2$. We extend the method to cases where $n(r)$ is a function that increases with r^2, leading to ray paths that can no longer be exclusively described by ellipses, but rather by a more general family of conics. Since the rays are in a plane, given the lens symmetry, the description of the paths can be limited to the xy plane without loss of generality. Using the corpuscular theory of light in Cartesian coordinates, Gutman showed [9] that the trajectories $x(\tau), y(\tau)$ of the light rays can be described by

$$\frac{d^2x}{d\tau^2} = c^2 \frac{\partial}{\partial x}\left(\frac{1}{2}n^2\right) \quad \text{and} \quad \frac{d^2y}{d\tau^2} = c^2 \frac{\partial}{\partial y}\left(\frac{1}{2}n^2\right) \tag{17}$$

with τ an arbitrary parameter and c the velocity of light in vacuum. This leads in our case to

$$\frac{d^2x}{d\tau^2} + c^2 b x = 0 \quad \text{and} \quad \frac{d^2y}{d\tau^2} + c^2 b y = 0 \tag{18}$$

If $b > 0$ i.e. if $\varepsilon_{center} > \varepsilon_{edge}$ the characteristic polynomial has imaginary roots $\pm jc\sqrt{b}$ leading to an expression taking the form (similar to [9])

$$\begin{cases} x(\tau) = \kappa_1 \cos(c\sqrt{b}\tau) + \kappa_2 \sin(c\sqrt{b}\tau) \\ y(\tau) = \kappa_3 \cos(c\sqrt{b}\tau) + \kappa_4 \sin(c\sqrt{b}\tau) \end{cases} \tag{19}$$

If $b < 0$ i.e. if $\varepsilon_{center} < \varepsilon_{edge}$ the characteristic polynomial has real roots $\pm c\sqrt{-b}$ leading to an expression taking the form

$$\begin{cases} x(\tau) = \kappa_1\ e^{(c\sqrt{-b}\tau)} + \kappa_2\ e^{(-c\sqrt{-b}\tau)} \\ y(\tau) = \kappa_3\ e^{(c\sqrt{-b}\tau)} + \kappa_4\ e^{(-c\sqrt{-b}\tau)} \end{cases} \tag{20}$$

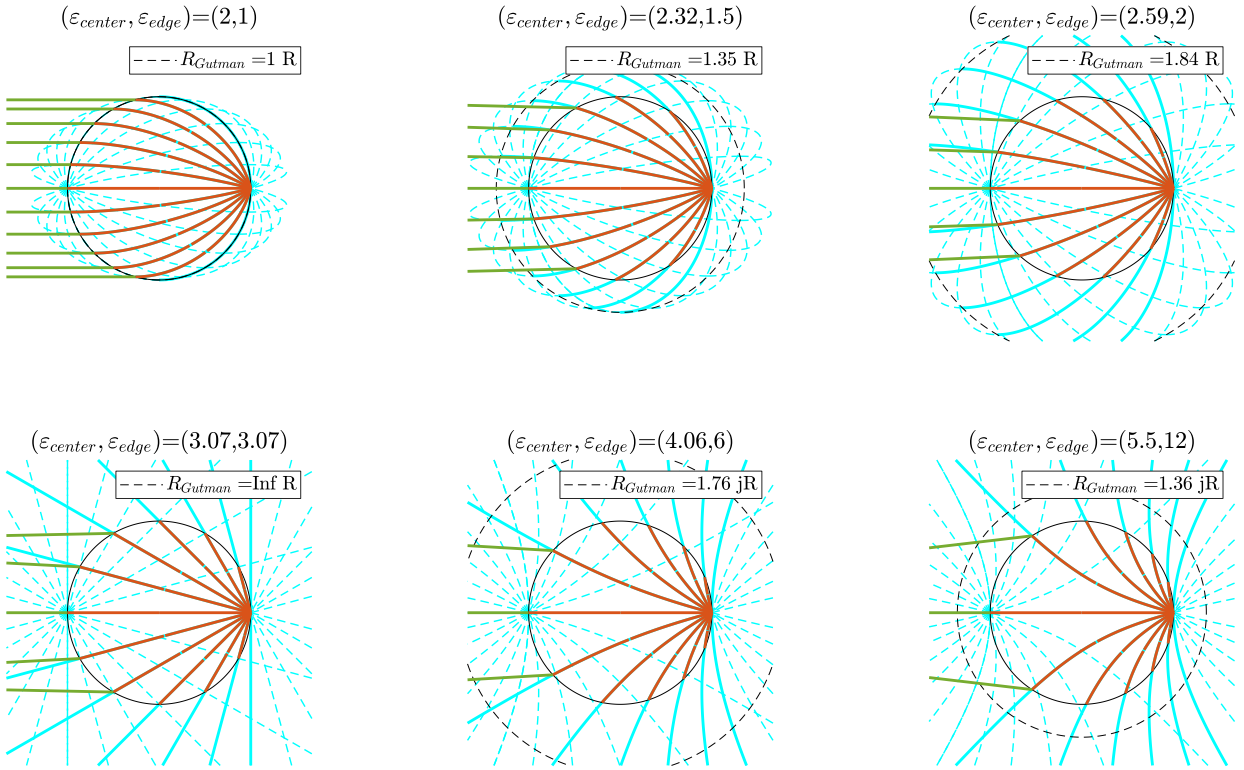

Fig. 2. Ray paths for different lenses obeying the empirical law (16). The new derivation of the ray path presented in Section II produces the orange trajectories split into the first and second parts (11), linked together by the point r_{min} (8) closest to the center. The computation of the *or* (15) gives the green trajectories outside the lens, for the rays which do not end up as internal reflections. The analytical expression (22) obtained in Section III as a generalization of Gutman's theory, produces the blue trajectories which are either ellipses, straight lines or hyperbolas. The radius R_{Gutman} is represented (in absolute value) by the dashed black circle, for the sake of comparison with the physical lens radius R represented by the solid black circle.

Authorized licensed use limited to: Univ Catholique de Louvain/UCL. Downloaded on June 24,2025 at 12:01:17 UTC from IEEE Xplore. Restrictions apply.
© 2025 IEEE. All rights reserved, including rights for text and data mining and training of artificial intelligence and similar technologies. Personal use is permitted, but republication/redistribution requires IEEE permission. See https://www.ieee.org/publications/rights/index.html for more information.

This article has been accepted for publication in IEEE Transactions on Antennas and Propagation. This is the author's version which has not been fully edited and content may change prior to final publication. Citation information: DOI 10.1109/TAP.2025.3572609

TABLE I
SUMMARY OF RAY TRAJECTORIES FOR THE DIFFERENT CASES.

Case	Classical Luneburg	Mismatched Luneburg lenses ($\varepsilon_{edge} > 1$)		
	$(\varepsilon_{center}, \varepsilon_{edge}) = (2, 1)$	$\varepsilon_{center} > \varepsilon_{edge}$	$\varepsilon_{center} = \varepsilon_{edge} = \varepsilon_{const}$	$\varepsilon_{center} < \varepsilon_{edge}$
Ray trajectories	Ellipses		Straight Lines	Hyperbolas
R_{Gutman}	Real		Infinite	Imaginary
$\lvert R_{Gutman}\rvert$	$\lvert R_{Gutman}\rvert = R$	$\lvert R_{Gutman}\rvert > R$		

One can determine the constants κ by imposing the boundary conditions, as done in [9], at $\tau = 0$ for the position and the initial orientation

$$\begin{cases} x(\tau=0) = R \text{ and } y(\tau=0) = 0 \\ \frac{dx}{d\tau}|_{\tau=0} = c\sqrt{a-b}\ \cos\alpha \text{ and } \frac{dy}{d\tau}|_{\tau=0} = c\sqrt{a-b}\ \sin\alpha \end{cases} \tag{21}$$

By eliminating the parameter τ, one eventually obtains in both (19)-(20) cases

$$\boxed{x(y) = y\ \frac{\cos\alpha}{\sin\alpha} \pm R\sqrt{1 - \left(\frac{y}{R_{Gutman}\ \sin\alpha}\right)^2}} \tag{22}$$

with a parameter that we call the *Gutman radius* given by

$$R_{Gutman} = R\ \sqrt{\frac{\varepsilon_{edge}}{\varepsilon_{center} - \varepsilon_{edge}}} \tag{23}$$

As long as $\varepsilon_{center} > \varepsilon_{edge}$, expression (22) is identical to (1), except that the focal point f in (1) is now replaced by the lens radius R, and the lens radius R in (1) by the Gutman radius R_{Gutman} which is such that $R_{Gutman} \geq R$. The lenses (4) under study therefore behave as *Truncated Gutman Lenses* with a truncation at the focal position (resulting in a source located on the lens physical perimeter). The elliptic trajectories would exit the lens in perfect collimation if they reached the radius R_{Gutman} of the non-truncated Gutman lens. In the *Truncated Gutman Lens*, they exit the lens at the physical radius R with partial collimation only (as in the virtual image lens in [13]), and the truncated part of the Gutman lens is replaced by a mismatch with the exterior medium (as in the hemispherical lens in [13]), providing an additional collimation effect. The combination of both effects provides optimal collimation. Such cases obeying the empirical law (16) with $\varepsilon_{edge} = 1$, 1.5 and 2 are represented in Fig. 2, where the ellipses are represented as blue curves.

When $\varepsilon_{center} < \varepsilon_{edge}$, expressions (22) and (1) remain very similar, except for a change of sign inside the square root, due to the Gutman radius becoming an imaginary number, which transforms the ray paths into hyperbolic trajectories. The lens now has a de-collimation effect, which can be optimally balanced by the collimation effect due to the mismatch with the exterior medium. Such cases obeying the empirical law (16) with $\varepsilon_{edge} = 6$ and 12 are represented in Fig. 2, where the hyperbolas are represented as blue curves.

One can note that the case $\varepsilon_{center} = \varepsilon_{edge}$ makes the Gutman radius infinite, making the square root term in (22) disappear. What remains is the equation of a family of straight lines, i.e. ray trajectories inside a transparent lens. In such a case, the lens has no collimation effect and the collimation is entirely obtained by the mismatch with the exterior medium. Such a case obeying the empirical law (16) with $\varepsilon_{edge} = 3.07$ is represented in Fig. 2, where the straight lines are represented as blue curves.

The different cases discussed in this section, resulting in ray paths which can be described either by ellipses, straight lines, or hyperbolas, are summarized in Table I.

IV. PHYSICAL OPTICS AND FREQUENCY DEPENDENCE

This section proposes to compute a radiation integral, in the context of physical optics, to combine the contributions of the different rays while taking into account frequency-dependent phase aberrations at the lens aperture. It goes beyond previous works that aimed at finding the optimal homogeneous dielectric lens fed on its perimeter, either through a minimization on average of the normalized phase aberrations [15] (normalized w.r.t. the lens diameter in wavelengths D/λ_0) leading to a discussion independent from the frequency, or through a full-wave analysis in cylindrical coordinates [16] using the SLL as performance indicator but limited to ratios $D/\lambda_0 \leq 9$.

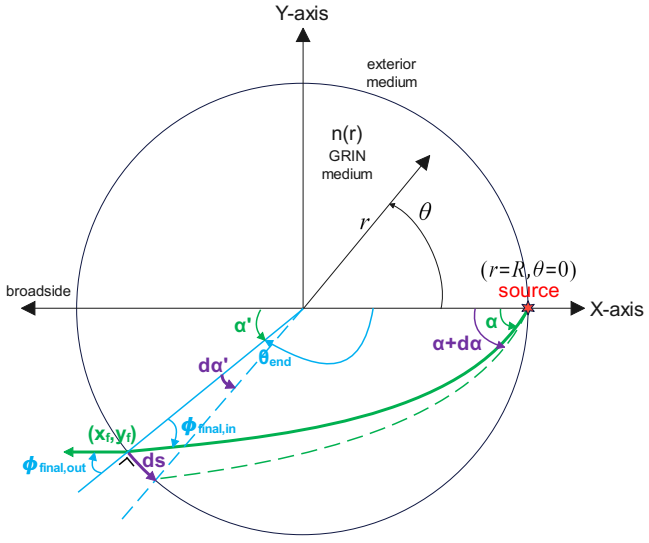

Fig. 3. Geometry of the physical optics problem. A ray path (green curve) starts with an initial angle α and exits the lens at (x_f, y_f) with an angular position given by angle α', both angles defined with respect to the main X-axis (broadside). Let us insist on the fact that α is an inscribed angle while α' is a central angle. An alternative ray path (dashed green curve) starting with an initial angle greater by $d\alpha$ exits the lens at an angular position greater by $d\alpha'$, resulting in a displacement ds along the lens aperture. The rays exit the lens with an angular deflection $\phi_{final,out}$ with respect to the normal to the infinitesimal planar surface defined by ds.

Authorized licensed use limited to: Univ Catholique de Louvain/UCL. Downloaded on June 24,2025 at 12:01:17 UTC from IEEE Xplore. Restrictions apply.
© 2025 IEEE. All rights reserved, including rights for text and data mining and training of artificial intelligence and similar technologies. Personal use is permitted, but republication/redistribution requires IEEE permission. See https://www.ieee.org/publications/rights/index.html for more information.

This article has been accepted for publication in IEEE Transactions on Antennas and Propagation. This is the author's version which has not been fully edited and content may change prior to final publication. Citation information: DOI 10.1109/TAP.2025.3572609

All rays are emitted at initial angle α and end up crossing the lens aperture at the position (x_f, y_f), obtained from (22), oriented with an angle $\alpha' = \pi - \theta_{end}$ with respect to broadside, see Fig. 3. Let us consider two adjacent rays, emitted with an infinitesimal difference $d\alpha$ in the initial angle and exiting the lens with an infinitesimal difference $d\alpha'$ in angular position, resulting in an infinitesimal displacement ds along the lens aperture (see Fig. 3). The rays exit the lens with an angular deflection $\phi_{final,out}$ with respect to the normal to the infinitesimal planar surface defined by ds.

In phased arrays, an equivalence can be found between the desired angular deflection of the main beam and the phase difference to be applied between elements [17]. Similarly, we focus here on the infinitesimal phase difference $d\varphi$ between fields on two points at the lens edge separated by a distance ds. We relate that phase difference with the known angular deflection $\phi_{final,out}$ of the ray at the lens edge:

$$d\varphi = k\ ds\ \sin\phi_{final,out} \Leftrightarrow \frac{d\varphi}{ds} = k\sqrt{\varepsilon_{edge}}\sin\alpha \qquad (24)$$

where (14) has been used, where $k = 2\pi/\lambda_0$ is the wavenumber and λ_0 the wavelength in free space. It is then possible to integrate the progressive phase differences to obtain an absolute phase φ for all points along the aperture (with the ray at broadside being the zero of the phase):

$$\varphi(\alpha^*) = \int_0^{s^*} \frac{d\varphi}{ds} ds = kR\sqrt{\varepsilon_{edge}} \int_0^{\alpha^*} \sin\alpha \left(\frac{d\alpha'}{d\alpha}\right) d\alpha \qquad (25)$$

since $ds = Rd\alpha' = R\frac{d\alpha'}{d\alpha}d\alpha$ (see Fig. 3). Using (13) and the fact that $d\alpha' = -d\theta_{end}$ it can be shown that

$$\frac{d\alpha'}{d\alpha} = 1 - \frac{\varepsilon_{center}(\varepsilon_{center} - 2\varepsilon_{edge})}{4\varepsilon_{edge}\sin^2\alpha(\varepsilon_{edge} - \varepsilon_{center}) + \varepsilon_{center}^2} \qquad (26)$$

We can eventually compute the radiation integral at broadside, summing the effect of all fields at the aperture. For that we take into account

- the propagation along their remaining path length $x_f + R$ in the broadside direction, before reaching the wavefront at $x = -R$,
- the absolute phase φ of each ray, linked to the angular deflections with respect to the normal to the aperture,
- the effect of the source intensity, included in a coefficient E_0 (taken equal to 1 in the following),
- the effect of the change of variable $d\alpha'/d\alpha$ as we integrate over the initial inscribed angles α instead of the central angles α' subtending the aperture,

and express the electric field at broadside as

$$E_{broadside} = E_0 \int_0^{\alpha_c} e^{j[k(R + x_f(\alpha)) - \varphi(\alpha)]} \left(\frac{d\alpha'}{d\alpha}\right) d\alpha \qquad (27)$$

where $\alpha_c = \sin^{-1}(1/\sqrt{\varepsilon_{edge}})$ is the critical angle above which rays end up in internal reflections.

The value of $E_{broadside}$ was computed for all possible combinations of $(\varepsilon_{center}, \varepsilon_{edge})$ and normalized to a maximum of 0 dB. Results are shown in Fig. 4 for $D/\lambda_0 = 6$ and in Fig. 5 for $D/\lambda_0 = 20$. Those results correspond to different frequencies for a fixed lens diameter, for example 60 GHz and 200 GHz for $D = 30$ mm.

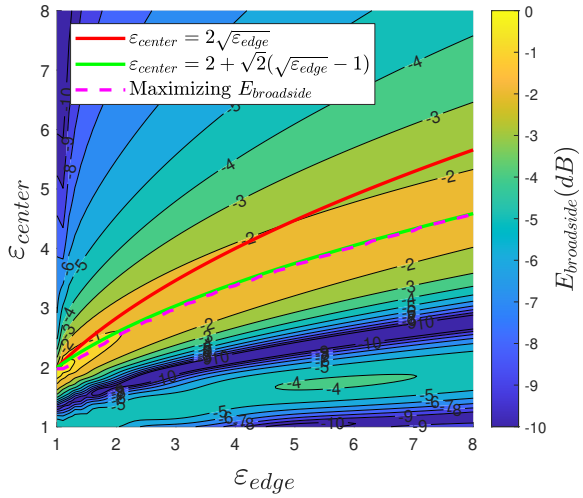

Fig. 4. $E_{broadside}$ (dB) obtained through physical optics for various combinations of $(\varepsilon_{center}, \varepsilon_{edge})$ assuming $D/\lambda_0 = 6$ (e.g. $f = 60$ GHz and $D = 30$ mm).

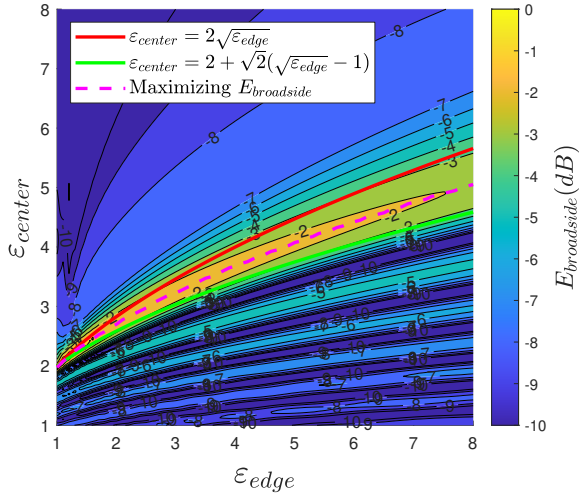

Fig. 5. $E_{broadside}$ (dB) obtained through physical optics for various combinations of $(\varepsilon_{center}, \varepsilon_{edge})$ assuming $D/\lambda_0 = 20$ (e.g. $f = 200$ GHz and $D = 30$ mm).

One can see that the distributions maximizing $E_{broadside}$ (dashed purple curve) under a ratio $D/\lambda_0 = 6$ perfectly superimpose with the empirical law (16). However, as this ratio increases, the distributions maximizing $E_{broadside}$ move away from the empirical law (16) (green curve) and get closer to the analytical law established with Abbe's refraction invariant (red curve) under the small angle approximation [12].

This observation is corroborated by full-wave simulations at $f = 200$ GHz with $D = 30$ mm, using the 2D cylindrical solver presented in [12]. The GRIN lens was discretized into 15 zones, a loss tangent of 0.0037 was considered, and the cylindrical harmonics $m \in [-200, 200]$ were computed. The gain was obtained for various combinations of $(\varepsilon_{center}, \varepsilon_{edge})$, as shown in Fig. 6. It can be seen that the distributions providing optimal gain follow the dashed purple curve that is located between the two laws (green and red curves) already mentioned.

Authorized licensed use limited to: Univ Catholique de Louvain/UCL. Downloaded on June 24,2025 at 12:01:17 UTC from IEEE Xplore. Restrictions apply.
© 2025 IEEE. All rights reserved, including rights for text and data mining and training of artificial intelligence and similar technologies. Personal use is permitted, but republication/redistribution requires IEEE permission. See https://www.ieee.org/publications/rights/index.html for more information.

This article has been accepted for publication in IEEE Transactions on Antennas and Propagation. This is the author's version which has not been fully edited and content may change prior to final publication. Citation information: DOI 10.1109/TAP.2025.3572609

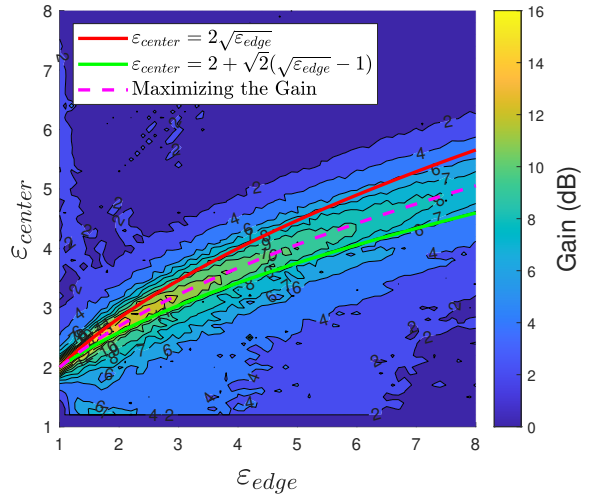

Fig. 6. Gain at $f = 200$ GHz, obtained through 2D full-wave simulations for a vertically polarized source placed on the perimeter of a lens of diameter $D = 30$ mm implementing various combinations of $(\varepsilon_{center}, \varepsilon_{edge})$.

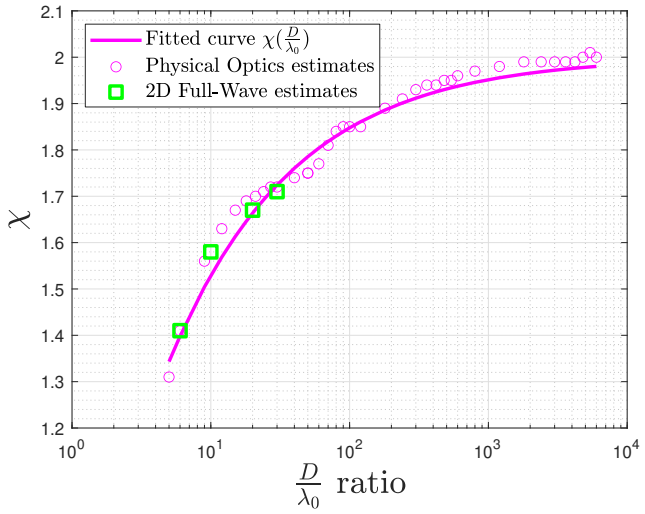

Fig. 7. Coefficient χ as a function of the ratio D/λ_0, shown as a fitted curve based on samples obtained with both physical optics and 2D full-wave.

This analysis was repeated for various D/λ_0 ratios. Irrespective of the ratio, and as expected from its analytical exactitude, the classical Luneburg lens $(\varepsilon_{center}, \varepsilon_{edge}) = (2, 1)$ is always part of the optimal distributions. Therefore, the curves of optimal distributions were fitted to the form

$$\boxed{\varepsilon_{center} = 2 + \chi(\sqrt{\varepsilon_{edge}} - 1)} \tag{28}$$

with χ a function of the ratio D/λ_0. The values of χ providing the best fit, sampled at various ratios D/λ_0, are shown in Fig. 7 as discrete circles when using physical optics (as in Fig. 4 and 5) and as discrete squares when using the full-wave solver (as in Fig. 6). Let us note that ratios above 30 could not be simulated in full-wave due to the large number of unknowns, leading to a badly conditioned system of equations. The evolution of the coefficient χ with the ratio D/λ_0 was fitted to the expression

$$\boxed{\chi = 0.16\frac{\lambda_0}{D} - 1.54\sqrt{\frac{\lambda_0}{D}} + 2} \tag{29}$$

shown in Fig. 7 as the solid purple line. A more precise fit, split into a high-frequency part (ratios $D/\lambda_0 \leq 50$) and a very high-frequency part (ratios $D/\lambda_0 \geq 50$), is discussed in Appendix A.

From the coefficient χ we can deduce the expression of the optimal homogeneous lens with constant relative dielectric permittivity ε_{const} as a function of the ratio D/λ_0, by solving equation (28) for $\varepsilon_{center} = \varepsilon_{edge} = \varepsilon_{const}$, which yields

$$\varepsilon_{const} = \left(\frac{\chi + \sqrt{\chi^2 - 4(\chi - 2)}}{2}\right)^2 \tag{30}$$

The corresponding curve ε_{const} based on the fitted expression (29) for χ is represented in Fig. 8.

Fig. 8 also shows full-wave simulation results that were obtained with the 2D cylindrical solver presented in [12]. For a lens of diameter $D = 30$ mm, homogeneous dielectric lenses with constant dielectric permittivity $2 < \varepsilon_r < 5$ were simulated at various frequencies between 50 GHz and 1.8 THz, corresponding to D/λ_0 ratios between 5 and 180. By using only 1 homogeneous dielectric zone, we were able to simulate at higher frequencies than in Fig. 7. The permittivity ε_{const} providing the maximum gain at each frequency was determined based on the raw data as well as smoothed data with different methods (Gaussian, median, mean, linear and quadratic regression). The green squares in Fig. 8 correspond to the mean of those estimates, while the uncertainty domain (green zone) covers all indicators from the minimum to the maximum estimates.

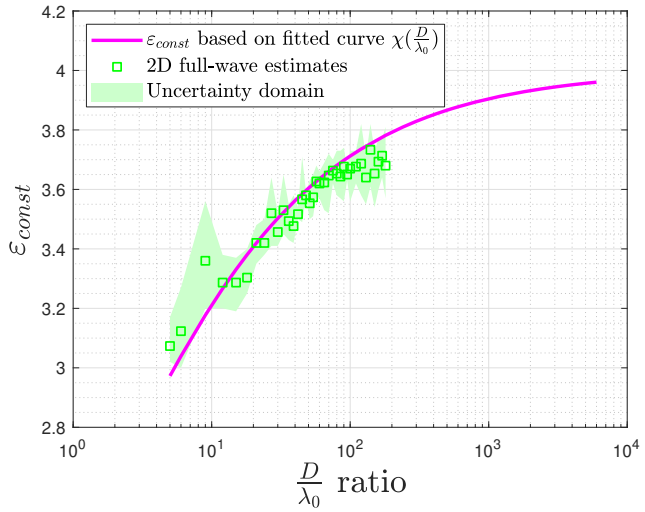

Fig. 8. Optimal homogeneous lens with constant relative dielectric permittivity ε_{const} as a function of the ratio D/λ_0. The green squares and zone were obtained through 2D full-wave simulations.

It can be observed that the full-wave estimates follow the fitted curve, especially at high frequencies. The uncertainty domain also gets smaller as the frequency increases (this is especially visible for ratios $D/\lambda_0 \geq 20$), as a consequence of the optimal zone getting narrower, as shown in Fig. 5 (ratio $D/\lambda_0 = 20$) with respect to Fig. 4 (ratio $D/\lambda_0 = 6$).

Authorized licensed use limited to: Univ Catholique de Louvain/UCL. Downloaded on June 24,2025 at 12:01:17 UTC from IEEE Xplore. Restrictions apply.
© 2025 IEEE. All rights reserved, including rights for text and data mining and training of artificial intelligence and similar technologies. Personal use is permitted, but republication/redistribution requires IEEE permission. See https://www.ieee.org/publications/rights/index.html for more information.

This article has been accepted for publication in IEEE Transactions on Antennas and Propagation. This is the author's version which has not been fully edited and content may change prior to final publication. Citation information: DOI 10.1109/TAP.2025.3572609

This section highlights the frequency dependence of *Mismatched Luneburg Lenses*:

- For ratios smaller than $D/\lambda_0 \approx 5$ the underlying assumptions related to the use of physical optics are not satisfied.
- For the ratio $D/\lambda_0 = 6$ that was studied in [12] ($f = 60$ GHz and $D = 30$ mm) the empirical law (16) obtained is consistent with the value $\chi = \sqrt{2}$ obtained from Fig. 7, to be introduced in (28). The constant lens case obtained from Fig. 8 is consistent with the value $\varepsilon_{const} = 3.07$ established in [12].
- For increasing ratios D/λ_0 the coefficient χ increases as well as ε_{const}, leading to optimal distributions moving away from the empirical law, as was observed in Fig. 5.
- For ratios close to $D/\lambda_0 \approx 30$, the coefficient reaches a value $\chi = \sqrt{3}$. The constant lens case obtained from Fig. 8 is consistent with the value $\varepsilon_{const} = 3.5$ established in [15] under a minimization of phase aberrations.
- For very high ratios reaching infinity, the asymptotic behaviour reaches $\chi = \sqrt{4} = 2$ and $\varepsilon_{const} = 4$, which are consistent with the law $\varepsilon_{center} = 2\sqrt{\varepsilon_{edge}}$ obtained with Abbe's refraction invariant [12], under the small angle approximation.

It had already been mentioned in the early literature [15][16] that $\varepsilon_{const} = 3.5$ appeared as the optimal value for a homogeneous lens fed on its perimeter, although a lens with ε_{const} anywhere between 3 and 4 would be quite adequate [16]. As now shown in Fig. 8, the optimal value in that interval is actually frequency-dependent.

According to Fermat's principle [18], the path of light between two points makes the optical length stationary with respect to variations of the path. Hence, rays exiting the lens parallel to each other are necessarily in phase. What about rays exiting the lens *almost* parallel to each other? The analysis based on ray tracing conducted in [12] showed that the distributions following (16) output rays featuring an orientation that has a standard deviation of about 5° with respect to broadside. This deviation produces a relative path difference that can be estimated by $1/\cos(5°) - 1 \approx 0.4\%$. Over the (maximum) remaining distance $D/2$ between the lens output and the wavefront, this deviation produces a relative phase error E^r_φ (relative to 2π) bounded by

$$E^r_\varphi < \frac{D}{\lambda_0}\, 0.2\% \tag{31}$$

which is similar to the value $0.004\ D/\lambda_0$ given in [15]. At small ratios such as $D/\lambda_0 = 6$ used in [12], the relative phase error is bounded by 1.2% of a 2π period, which remains small. In this case, rays practically parallel to each other are de facto practically in phase as well (hence we refer to it as the *angular regime*). This explains why the method based on ray tracing (frequency-independent) and the full-wave method (frequency-dependent) gave essentially the same optimal distributions in [12]. However, as the ratio D/λ_0 increases, this equivalence is no longer valid, and phase aberrations increase. At some point the distributions reach a constant case with $\varepsilon_{const} = 3.5$ established in [15] by minimization of the phase aberrations (we refer to it as the *aberrations regime*). For very large D/λ_0 ratios, the phase aberrations become so large that destructive interference takes place for the majority of rays with large initial angle α, up to the point, for $D/\lambda_0 \to \infty$, where it takes place for all rays with $\alpha \neq 0$ (we refer to it as the *paraxial regime*). This explains why the optimal distributions asymptotically move towards the law obtained with Abbe's refraction invariant [12] under the small angles approximation.

To sum up, we can identify three regimes of operation, as shown in Table II.

TABLE II
SUMMARY OF THE THREE REGIMES OF OPERATION.

Regime	D/λ_0	χ	ε_{center}	ε_{const}
Angular	$= 6$	$\sqrt{2}$	$2+\sqrt{2}\ (\sqrt{\varepsilon_{edge}}-1)$	3.07
Aberrations	≈ 30	$\sqrt{3}$	$2+\sqrt{3}\ (\sqrt{\varepsilon_{edge}}-1)$	3.5
Paraxial	$\to \infty$	$\sqrt{4}$	$2+\sqrt{4}\ (\sqrt{\varepsilon_{edge}}-1)$	4

V. 3D Simulations and Comparisons

In [13], the authors proposed to combine the principles of a virtual image lens – i.e. a lens providing partial collimation only – and an extended hemispherical lens – i.e. a lens relying on the interface effect with the exterior medium. Similarly, the *Mismatched Luneburg Lenses* proposed here rely on a GRIN lens coupled to a mismatched interface with the exterior medium. It was shown in Section III that such lenses can be viewed as *Truncated Gutman Lenses*, hence providing partial collimation only, while Section IV showed that the interface effect is actually frequency-dependent. This section aims at highlighting the importance of the latter, through 3D simulations.

The refractive index distributions $n_{vi}(r)$ providing a given virtual image lens are obtained in [13] by solving an integral equation, which is exact for all rays. Then, the distributions are denormalized by the refractive index n_h obtained as the inverse of the eccentricity of a homogeneous elliptical lens; the ellipse must have its far focal point located at the virtual image point, and must fit the lens circular aperture in a least-square error sense, if one wants to maintain the rotational symmetry of the device. The resulting distributions $n_{vi}(r) \cdot n_h$ produce rays that are quasi-parallel at the output of the lens, yet they feature some spherical aberration.

The *Collimating Truncated Virtual Image Lens* method presented in [13] was applied for various virtual image positions (moving from the lens perimeter to infinity). The resulting dielectric distributions are shown in yellow in Fig. 9: they move between the classical Luneburg lens ($n_{vi}(r) = \sqrt{2 - r^2}$ and $n_h = 1$), plotted as a black curve, and a constant lens ($n_{vi}(r) = 1$ and $n_h = \sqrt{3.31}$). The derivation, based on geometrical optics (GO), produces lenses that are supposedly frequency-independent by design [13]. Those distributions are compared with those described in our previous work [12] which are now shown to correspond to a ratio $D/\lambda_0 = 6$ (light blue curves in Fig. 9), as well as other *Mismatched Luneburg Lens* distributions described in this work (obtained from (28) and (29)), corresponding to larger ratios $D/\lambda_0 = 20$ (dark blue curves in Fig. 9), $D/\lambda_0 = 50$ (purple curves in Fig. 9) and $D/\lambda_0 \to \infty$ (red curves in Fig. 9).

Authorized licensed use limited to: Univ Catholique de Louvain/UCL. Downloaded on June 24,2025 at 12:01:17 UTC from IEEE Xplore. Restrictions apply.
© 2025 IEEE. All rights reserved, including rights for text and data mining and training of artificial intelligence and similar technologies. Personal use is permitted, but republication/redistribution requires IEEE permission. See https://www.ieee.org/publications/rights/index.html for more information.

This article has been accepted for publication in IEEE Transactions on Antennas and Propagation. This is the author's version which has not been fully edited and content may change prior to final publication. Citation information: DOI 10.1109/TAP.2025.3572609

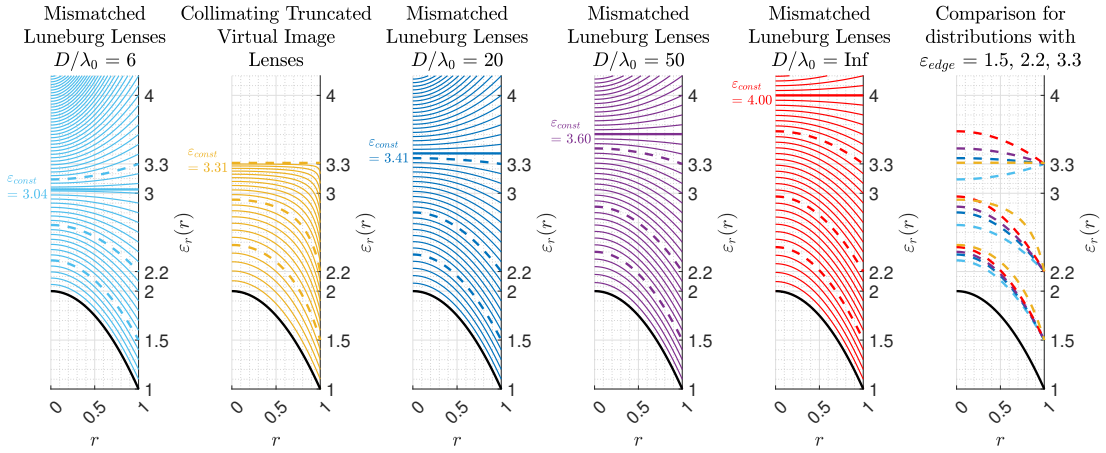

Fig. 9. Comparison between the *Collimating Truncated Virtual Image Lens* distributions (yellow curves) and *Mismatched Luneburg Lens* distributions corresponding to ratios $D/\lambda_0 = 6$ (light blue curves), $D/\lambda_0 = 20$ (dark blue curves), $D/\lambda_0 = 50$ (purple curves) and $D/\lambda_0 \to \infty$ (red curves).

Distributions featuring three levels of mismatch, i.e. an $\varepsilon_{edge} = n_h^2 = 1.5$, 2.2 and 3.3, were considered for pattern simulations, and are highlighted in Fig. 9 as dashed curves. The 3D simulations were conducted with the CST commercial software [19] for a cylindrical GRIN lens with a diameter $D = 30$ mm, discretized into 15 homogeneous dielectric zones. The lens was excited on its perimeter by a discrete port acting as a vertically polarized current source at frequencies $f = 60$ GHz ($D/\lambda_0 = 6$), $f = 200$ GHz ($D/\lambda_0 = 20$) and $f = 500$ GHz ($D/\lambda_0 = 50$). The lens was placed between metallic plates with a thickness h maintained constant w.r.t. the wavelength λ_0, with a ratio $h/\lambda_0 = 0.4$ (i.e. $h = 2$ mm at 60 GHz, 0.6 mm at 200 GHz and 0.24 mm at 500 GHz). The simulated structures can be seen at the top of Fig. 10.

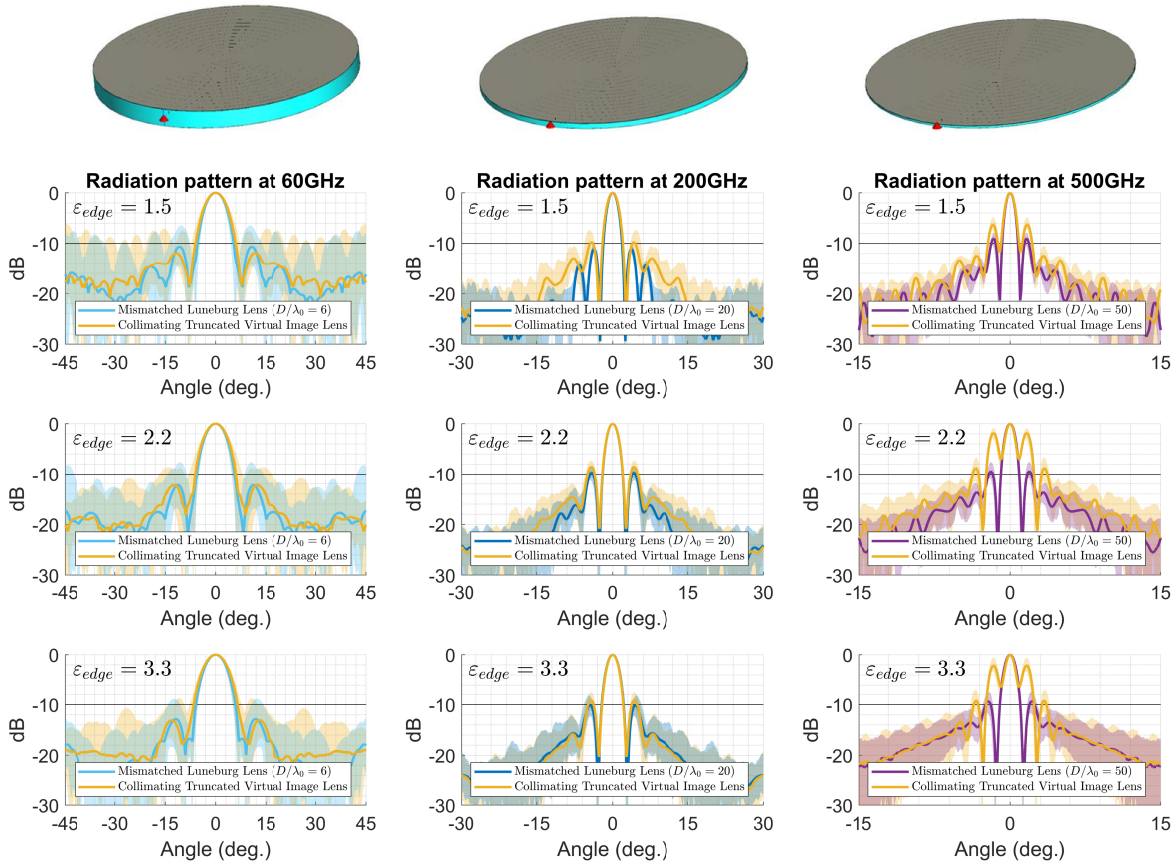

Fig. 10. Radiation patterns obtained at $f = 60$ GHz (left column), 200 GHz (central column) and 500 GHz (right column), for GRIN lens structures (first line, with metal in dark grey and dielectric substrate in blue) featuring an $\varepsilon_{edge} = 1.5$ (second line), $\varepsilon_{edge} = 2.2$ (third line) and $\varepsilon_{edge} = 3.3$ (last line). The solid curves correspond to the average patterns, while the shaded zones correspond to the variation within a 10 GHz bandwidth.

Authorized licensed use limited to: Univ Catholique de Louvain/UCL. Downloaded on June 24,2025 at 12:01:17 UTC from IEEE Xplore. Restrictions apply.
© 2025 IEEE. All rights reserved, including rights for text and data mining and training of artificial intelligence and similar technologies. Personal use is permitted, but republication/redistribution requires IEEE permission. See https://www.ieee.org/publications/rights/index.html for more information.

This article has been accepted for publication in IEEE Transactions on Antennas and Propagation. This is the author's version which has not been fully edited and content may change prior to final publication. Citation information: DOI 10.1109/TAP.2025.3572609

Each time, frequencies covering a 10 GHz bandwidth around the central frequency, with a step of 1 GHz, were considered. The simulated radiation patterns in the collimation plane are shown in Fig. 10: the solid curves correspond to the average pattern over that bandwidth, while the shaded zones correspond to the variation within that bandwidth. The performance obtained with the lenses described in [13] (yellow curves) is compared at each frequency with the *Mismatched Luneburg Lens* (MLL) corresponding to the appropriate D/λ_0 ratio (light blue, dark blue or purple curves). The mean performance in each case is also given in Table III in terms of SLL and gain. The following observations can be made:

- Both methods – the one given in [13] and the one we proposed in [12] – provide a similar performance at 60 GHz ($D/\lambda_0 = 6$) for all three levels of mismatch considered (see left column in Fig. 10). This case corresponds to the *angular regime* established in Section IV, where rays practically parallel are also practically in phase. On the average, the SLL is 0.32 dB higher and the gain 0.04 dB lower with the distributions from [13].
- As the frequency increases to 200 GHz ($D/\lambda_0 = 20$), one can observe slight differences in performance between the method given in [13] and the extended method we proposed in this work, for all three levels of mismatch considered (see central column in Fig. 10). The difference is negligible for $\varepsilon_{edge} = 3.3$ since both methods provide a similar and quasi-constant distribution. This case is close to the *aberrations regime* established in Section IV where phase aberrations start to become critical. On the average, the SLL is 1.18 dB higher and the gain 0.59 dB lower with the distributions from [13].
- As the frequency reaches $f = 500$ GHz ($D/\lambda_0 = 50$), a significant difference is observed between the method given in [13] and the frequency-dependent method proposed in this work, for all three levels of mismatch considered (see right column in Fig. 10). The increase in SLL and decrease in gain with the GO-based method [13] is significant, especially at larger levels of mismatch. This case approaches the *paraxial regime* established in Section IV in which phase aberrations result in destructive interference for the majority of rays with large initial angle α. On the average, the SLL is 5.84 dB higher and the gain 1.96 dB lower with the distributions from [13].

Experimental demonstrations of *Mismatched Luneburg Lens* designs on PCB at 60 GHz ($D/\lambda_0 = 6$) can be found in our previous works [20] ($\varepsilon_{edge} = 2.6$) and [21] ($\varepsilon_{edge} = 2.2$), providing stable radiation patterns over a bandwidth as large as 10 GHz. The authors in [13] also provide an experimental validation of their method for a lens ($n_h^2 = 1.56 \approx \varepsilon_{edge}$) fabricated through additive manufacturing and measured at 30 GHz ($D/\lambda_0 = 8$). The simulations conducted in this section show that the extended description of *Mismatched Luneburg Lenses* given here, including their frequency dependence established in Section IV, allows designers to implement mismatched lenses that maintain low SLL even at very large D/λ_0 ratios, unlike design methods relying on classical GO without phase information.

TABLE III
FULL-WAVE COMPARISON: SLL AND GAIN.

	$f = 60$ GHz $D/\lambda_0 = 6$		$f = 200$ GHz $D/\lambda_0 = 20$		$f = 500$ GHz $D/\lambda_0 = 50$	
	MLL	[13]	MLL	[13]	MLL	[13]
	SLL (dB) averaged over the 10 GHz bandwidth					
$\varepsilon_{edge} = 1.5$	-10.17	-9.93	-11.04	-9.61	-8.99	-6.24
$\varepsilon_{edge} = 2.2$	-11.46	-10.82	-9.54	-8.40	-9.38	-1.81
$\varepsilon_{edge} = 3.3$	-12.01	-11.93	-9.99	-9.03	-9.30	-2.12
Mean diff.	**+0.32**		**+1.18**		**+5.84**	
	Gain (dB) averaged over the 10 GHz bandwidth					
$\varepsilon_{edge} = 1.5$	12.92	12.94	17.88	16.55	18.43	16.90
$\varepsilon_{edge} = 2.2$	13.02	13.14	16.94	16.49	17.27	14.49
$\varepsilon_{edge} = 3.3$	13.26	12.99	16.61	16.63	15.88	14.33
Mean diff.	**-0.04**		**-0.59**		**-1.96**	

VI. CONCLUSION

We have provided an analytical expression for the ray paths inside any GRIN lens featuring a refractive index following a square law radially. The derivation is immediate, based on the conservation of the angular momentum. We have then shown that such a GRIN lens could be seen as a *Truncated Gutman Lens* with a physical lens radius different from the *Gutman radius* of the non-truncated Gutman lens. The extension of Gutman's theory shows that the ray paths are a family of conics, either ellipses, straight lines or hyperbolas. We then used those ray paths to compute a radiation integral using physical optics, which highlighted the frequency dependence of the optimal distributions, leading to a generalized rule in the form

$$\varepsilon_{center} = 2 + \chi\ (\sqrt{\varepsilon_{edge}} - 1)$$

with χ a function of the ratio D/λ_0. That frequency dependence was corroborated by 2D full-wave simulations. We eventually showed the importance of that frequency dependence through 3D full-wave simulations, highlighting the limits of mismatched lenses designed in a frequency-independent framework.

The authors believe that this paper can prove useful to GRIN lens designers, including those designing homogeneous lenses. The empirical rules provided here are straightforward and simple to use. In [12] it was advocated that a mismatch at the lens edge could ease practical realizations and increase design flexibility, as demonstrated with practical realizations on PCB at V-band in [20][21]: this paper further emphasizes the deliberate nature of such a choice, by highlighting that the frequency is to be considered in the design of a *Mismatched Luneburg Lens*.

ACKNOWLEDGMENT

This work was conducted thanks to the collaboration between the ICTEAM Research Group (Université catholique de Louvain) and BEA Sensors Europe, and was funded by the Région Wallonne under the "Doctorat en entreprise" framework of the SPW EER.

Authorized licensed use limited to: Univ Catholique de Louvain/UCL. Downloaded on June 24,2025 at 12:01:17 UTC from IEEE Xplore. Restrictions apply.
© 2025 IEEE. All rights reserved, including rights for text and data mining and training of artificial intelligence and similar technologies. Personal use is permitted, but republication/redistribution requires IEEE permission. See https://www.ieee.org/publications/rights/index.html for more information.

This article has been accepted for publication in IEEE Transactions on Antennas and Propagation. This is the author's version which has not been fully edited and content may change prior to final publication. Citation information: DOI 10.1109/TAP.2025.3572609

APPENDIX A
BIFURCATION PHENOMENON

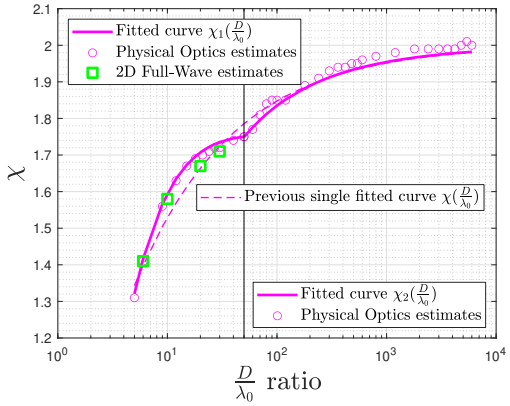

Fig. 11. Coefficient χ as a function of the ratio D/λ_0. There are two fitted curves χ_1 and χ_2, corresponding to the regions $D/\lambda_0 \leq 50$ and $D/\lambda_0 \geq 50$.

A more precise fit, split into a high-frequency (ratios $D/\lambda_0 \leq 50$) and a very high-frequency (ratios $D/\lambda_0 \geq 50$) parts, is mentioned here:

$$\begin{cases} \chi_1 = -3.93\dfrac{\lambda_0}{D} + 0.91\sqrt{\dfrac{\lambda_0}{D}} + 1.7 & \text{for } \dfrac{D}{\lambda_0} \leq 50 \\ \chi_2 = -3.00\dfrac{\lambda_0}{D} - 1.35\sqrt{\dfrac{\lambda_0}{D}} + 2.0 & \text{for } \dfrac{D}{\lambda_0} \geq 50 \end{cases} \tag{32}$$

This new fit is represented in Fig. 11 along with the previous single fitted curve (29). This split would imply a bifurcation phenomenon taking place around ratios $D/\lambda_0 \approx 50$, close to the values $\chi \approx \sqrt{3}$ and $\varepsilon_{const} \approx 3.5$, the latter being mentioned multiple times in the literature [15][16] as a solution minimizing phase aberrations. It can be shown that above such ratios, the phasors $e^{j[k(R+x_f(\alpha))-\varphi(\alpha)]}$ in (27) go beyond $\pm\pi/2$ for some initial angles α, meaning the start of destructive interference, and the apparent change of behaviour.

REFERENCES

[1] R. K. Luneburg, *Mathematical theory of optics*, Berkeley, CA, USA: Univ. California Press, 1964.

[2] T. J. Prince, M. A. Elmansouri, and D. S. Filipovic, "Cylindrical Luneburg lens antenna systems for amplitude-only direction-finding applications," *IEEE Trans. Antennas Propag.*, vol. 71, no. 10, pp. 7924-7932, Oct. 2023.

[3] C. Babayigit, A. S. Evren, E. Bor, H. Kurt, and M. Turduev, "Analytical, numerical, and experimental investigation of a Luneburg lens system for directional cloaking," *Phys. Rev. A*, vol. 99, no. 4, Apr. 2019.

[4] A. Mahmoud *et al.*, "Low-cost and low-profile sub-terahertz Luneburg lens beamformer on polymer," *IEEE Antennas Wireless Propag. Letters*, vol. 22, no. 6, pp. 1411-1415, June 2023.

[5] B. Nie, H. Lu, T. Skaik, Y. Liu, and Y. Wang, "A 3D-printed subterahertz metallic surface-wave Luneburg lens multibeam antenna," *IEEE Trans. Terahertz Science and Technology*, vol. 13, no. 3, pp. 297-301, May 2023.

[6] J. Li *et al.*, "Design of a broadband metasurface Luneburg lens for full-angle operation," *IEEE Trans. Antennas Propag.*, vol. 67, no. 4, pp. 2442-2451, Apr. 2019.

[7] C. Bilitos *et al.*, "Higher-symmetries for broadband reflecting Luneburg lenses at Ka-band," in *Proc. 16th Eur. Conf. Antennas Propag. (EuCAP)*, Madrid, Spain, Mar. 2022, pp 1-3.

[8] W. Yu, X. Wang, H. Lu, H. Liu, and C. Jin, "3D-printed all-metal terahertz multibeam lens antenna based on photonic crystal," in *IEEE Access*, vol. 11, pp. 41609-41617, 2023.

[9] A. S. Gutman, "Modified Luneburg lens," *J. Appl. Phys.*, vol. 25, no. 7, pp. 855-859, July 1954.

[10] J. A. Lock, "Scattering of an electromagnetic plane wave by a Luneburg lens. I. Ray theory," *J. Opt. Soc. Am. A*, vol. 25, no. 12, pp. 2971-2979, 2008.

[11] J. Ruiz-García, E. Martini, C. D. Giovampaola, D. González-Ovejero, and S. Maci, "Reflecting Luneburg lenses," *IEEE Trans. Antennas Propag.*, vol. 69, no. 7, pp. 3924–3935, Jul. 2021.

[12] V. Kaschten, D. Tihon, D. Lederer, and C. Craeye, "Mismatched Luneburg lenses: numerical analysis and design rules," *IEEE Trans. Antennas Propag.*, vol. 72, no. 5, pp. 4487-4500, May 2024.

[13] O. Zetterstrom, N. J. G. Fonseca, and O. Quevedo-Teruel, "Collimating truncated virtual image lens," *IEEE Trans. Antennas Propag.*, vol. 72, no. 5, pp. 3928-3937, May 2024.

[14] N. J. G. Fonseca, T. Tyc, and O. Quevedo–Teruel, "A solution to the complement of the generalized Luneburg lens problem," *Commun. Phys.*, vol. 4, no. 1, Dec. 2021.

[15] T. C. Cheston, and E. J. Luoma, "Constant-K lenses," *Johns Hopkins APL Tech. Dig.*, vol. 2, no. 4, pp. 8-11, Mar./Apr. 1963.

[16] L. Gunderson, "An electromagnetic analysis of a cylindrical homogeneous lens," *IEEE Trans. Antennas Propag.*, vol. 20, no. 4, pp. 476-479, July 1972.

[17] P. F. McManamon *et al.*, "Optical phased array technology," in *Proc. IEEE*, vol. 84, no. 2, pp. 268-298, Feb. 1996.

[18] M. Born, and E. Wolf, *Principles of optics*, 7th ed. Cambridge, U.K.: Cambridge Univ. Press, 1999.

[19] CST Studio Suite, Electromagnetic field simulation software, Dassault Systems.

[20] V. Kaschten, D. Lederer, and C. Craeye, "A cylindrical mismatched Luneburg lens implemented on PCB at V-band," in *Proc. 18th Eur. Conf. Antennas Propag. (EuCAP)*, Glasgow, U.K., Mar. 2024, pp 1-5.

[21] V. Kaschten, D. Lederer, and C. Craeye, "Metallic elements inside a mismatched Luneburg lens: experimental validation at V-band," in *Proc. 19th Eur. Conf. Antennas Propag. (EuCAP)*, Stockholm, Sweden, Mar. 2025, pp 1-5.

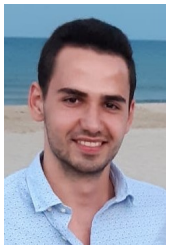

Vincent Kaschten received the B.S and M.S in Electrical Engineering from Université de Liège (ULiège), Liège, Belgium, in 2018 and 2020 respectively. Since 2021, he is pursuing a Ph.D. at Université catholique de Louvain (UCLouvain), Louvain-la-Neuve, Belgium, in the Institute of Information and Communication Technologies, Electronics and Applied Mathematics (ICTEAM), in collaboration with the company BEA Sensors, and under a funding by the Région Wallonne under the "Doctorat en entreprise" framework of the SPW EER.

Dimitri Lederer received M.S. and Ph.D. degrees in applied sciences from UCLouvain, Louvain-la-Neuve, Belgium, in 2000 and 2006, respectively.nAfter completing his Ph.D. in the field of SOI material and device characterization for microwave applications he worked in various SMEs and large-scale companies on the development of RF & microwave and sub-THz products. Prior to joining UCLouvain in 2019, he worked as a Senior Engineer at GlobalFoundries, where he worked on the development of the 45RFSOI technology. His research interests cover the modeling, fabrication, design, and characterization of Si-based technologies, devices, and circuits for sub-THz and THz applications. Prof. Lederer has published more than 100 papers in peer-reviewed journals and conference proceedings.

Christophe Craeye received the Electrical Engineer in 1994 and the Ph.D. degree in microwave remote sensing in 1998, both from Université catholique de Louvain (UCLouvain), Louvain-la-Neuve, Belgium. From 1999 to 2001, he stayed as a post-doc researcher in The Netherlands, in the framework of the Square Kilometer Array radio telescope project. He is currently a professor at UCLouvain. His research topics are multiple-antenna systems and metamaterials. Dr. Craeye served as an Associate Editor for several IEEE journals between 2004 and 2017.

Authorized licensed use limited to: Univ Catholique de Louvain/UCL. Downloaded on June 24,2025 at 12:01:17 UTC from IEEE Xplore. Restrictions apply.
© 2025 IEEE. All rights reserved, including rights for text and data mining and training of artificial intelligence and similar technologies. Personal use is permitted, but republication/redistribution requires IEEE permission. See https://www.ieee.org/publications/rights/index.html for more information.